Review Article **Open Access**

Mohammed Ali Benhamida, Hamza Ennassiri*, Yacine Amara, and Georges Barakat

Reluctance network lumped mechanical & thermal models for the modeling and predesign of concentrated flux synchronous machine

https://doi.org/10.1515/phys-2018-0088
Received November 2, 2017; accepted December 1, 2017

Abstract: The aim of this paper is the multi-physical modeling of synchronous permanent magnet machines, dedicated to hybrid electrical vehicles application, using reluctance network lumped mechanical and thermal models. The modeling approaches are presented and validated by comparing the obtained results to those of finite element method with a close look to the airgap modeling and the consideration of soft magnetic materials non-linearity in the electromagnetic modeling. As well as a close look also on the conduction and convection heat coefficients for the machine different regions in the thermal modeling. Finally a focus on the mass, damping and stiffness matrix computation in lumped mechanical modeling taking into account the temperature influence on the materials mechanical properties. In addition a simplified rotating electrical machine is described and multiple coupled analysis were done in order to derive the structure magneto-vibro-acoustic performances.

Keywords: Reluctance network, lumped mechanical model, lumped thermal model, hybrid electrical vehicles, electromagnetic modeling, vibration & noise due to electromagnetic origin

PACS: 43.40.+s; 44.05.+e; 46.40.-f; 41.20.-q

1 Introduction

This paper presents multi-physical models devoted to the pre-design of a concentrated flux embedded permanent magnet (CFPM) dedicated to electric vehicles (EV). The choice of this structure is mainly based on its characteristics which must fulfill the requirements of an EV [1, 2] drive system such as, high torque, high power density, high efficiency over large speed and torque ranges, low acoustic emissions and low torque ripple. The pre-design of the CFPM motor is done using a developed reluctance network coupled to lumped mechanical and thermal models for the investigation of electromagnetic and vibrational performances. The models are presented and validated by comparing the obtained results to those of finite elements method. The main parameters and geometry of the studied machine are given respectively in Table 1 and Figure 1.

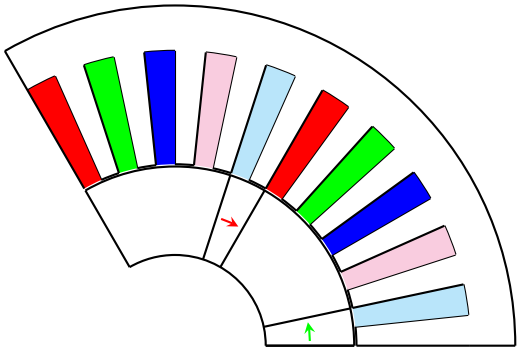

Figure 1: Presentation of the studied 30 slots/3poles machine

Mohammed Ali Benhamida: Groupe de Recherche en Électrotechnique et Automatique du Havre (GREAH- EA3220), Le Havre University, France E-mail: benhamida.mohammed.ali@gmail.com
Yacine Amara, Georges Barakat: Groupe de Recherche en Électrotechnique et Automatique du Havre (GREAH- EA3220), Le Havre University, France
***Corresponding Author: Hamza Ennassiri:** Groupe de Recherche en Électrotechnique et Automatique du Havre (GREAH - EA-3220), Le Havre University, France, E-mail: hamza.ennassiri@free.fr

2 Reluctance network (RN)

In order to develop the interpolation based reluctance network electromagnetic model some assumptions were made for reducing its complexity [3]. First, the magnetic

Table 1: Machine's main parameters

Phases	5
Poles / Slots	6/30
air gap radius	85 mm
Magnet's height	18.7 mm
Magnet's aperture angle	8 deg
Slot's height	47.3 mm
Stator yoke thickness	24 mm
Airgap	1 mm
Slot's aperture angle	5.8 deg
Active axial length	107 mm
Phase Number	5
Filling factor	0.6
Current density	4 A.mm^{-2}
Ω	3000 rpm

field in the structure is considered bidirectional, which reduces the problem into a 2-D modeling where the equation are developed in a cylindrical coordinate system, second a tangential magnetic field boundary condition will be applied to the external air surrounding the machine and third the magnetic materials are supposed to be homogeneous, isotropic, temperature free characterized by there linear B(H) curve. Last, a magneto-static system is assumed, thus eddy current and hysteresis are neglected.

In reluctance network an equivalence is done between the magnetic equivalent circuit MEC and the electrical one [4], where the magnetic flux is the current and the nodal magnetic scalar potential is the voltage. Figure 2 exposes the elementary block represented by cylindrical bidirectional reluctance for the modeling of radial machine [5].

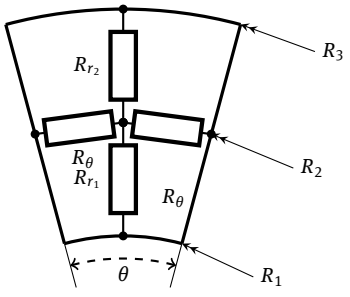

Figure 2: Representation of an elementary block with cylindrical bidirectional reluctances

The RN method results in a set of linear equations given by Eq. (1) which should be solved to obtain magnetic scalar potentials.

$$[P].[U] = [\phi]. \tag{1}$$

Where [P] (**nn**-**m** x **nn**) is the permeances matrix; [ϕ] (**nn** x 1) is the excitation vector, elements of which are related to geometry distribution and physical properties of magnetic field sources (magnetic remanence and current density distributions) and [U] (**nn** x 1) is the unknowns vector (the magnetic scalar potentials in each node). **nn** is the number of total nodes in the reluctance network and **m** is the number of nodes located in the sliding surface positioned in the air-gap. The **m** missing equation in the matrix system will be provided by the air gap modeling method, which will be discussed next section.

In a radial field machine, the computation of the two reluctance R_r and R_θ, which are respectively the radial and circumferential magnetic reluctance is done on a cylinder portion located between two radius (an outer one R_3 and an inner one R_1, R_2 is the mean value of the two last radii), with an angular aperture equal to θ, L_a is the machine active length and μ_r is the relative permeability of the corresponding region. The reluctance formulation is given by Eq. (2).

$$\begin{cases} R_{r_1} = \log\left(\dfrac{R_2}{R_1}\right)\dfrac{1}{\mu_0\mu_r\theta L_a} \\ R_{r_2} = \log\left(\dfrac{R_3}{R_2}\right)\dfrac{1}{\mu_0\mu_r\theta L_a} \\ R_\theta = \dfrac{\theta}{2\mu_0\mu_r L_a \log\left(\dfrac{R_3}{R_1}\right)} \end{cases} \tag{2}$$

2.1 Airgap modeling

The airgap will be modeled by nodal interpolation functions, which take into consideration the continuity of the magnetic scalar potential and the magnetic flux density at the surface of the sliding region, which is the surface separating the moving parts from the static one. Let's assume a rotor node located in the sliding surface is sandwiched between two nodes associated to the stator having θ_r,θ_{s1} and θ_{s2} as circumferential coordinates and U_r,U_{s1} and U_{s2} as nodal scalar potential respectively, as can be seen in Figure 3. The potential located in the rotor can be written in function of the two placed in the stator by using first order Lagrange interpolation:

$$U_r = \frac{(\theta_r - \theta_{s1})}{(\theta_{s2} - \theta_{s1})}U_{s2} + \frac{(\theta_r - \theta_{s2})}{(\theta_{s1} - \theta_{s2})}U_{s1}. \tag{3}$$

With the previous equation we assume that the potential has a linear shape between two successive nodes. This assures the equality of the scalar potential at the sliding surface, which will provide the missing M_{rt} equations for the

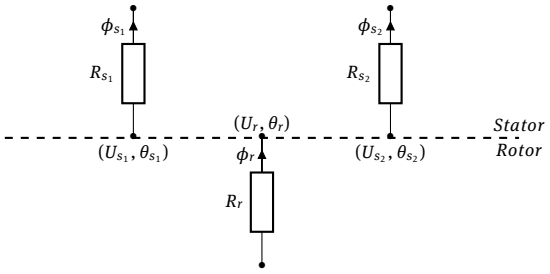

Figure 3: Scalar potential interpolation at the sliding surface

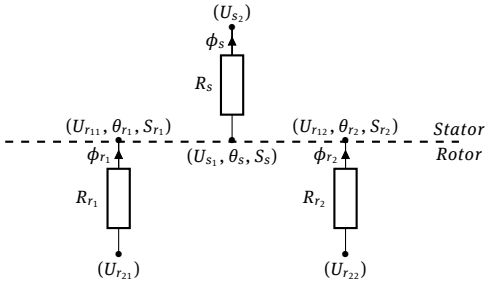

Figure 4: Magnetic flux density interpolation at the sliding surface

rotor. In general the previous equation can be generalized and written in a matricial system as follows:

$$[U_r] - [M_{strt}][U_s] = 0 \tag{4}$$

With $[U_r\ ]\ [U_s]$ are the vectors containing rotor and stator potentials corresponding to the nodes located at the sliding surfaces. $[M_{strt}]$ is the interpolation matrix.
To satisfy the second interface condition; which is the continuity of the magnetic flux density, and provide the missing M_{st} equation for the stator, the magnetic flux density continuity between the two reluctance networks will be assured by using the same interpolation method employed previously. In this case stator's magnetic flux density will be written in function of the rotor's one. As the previous step, let's assume that a node belonging to the stator and located in the sliding surface is sandwiched between two nodes associated to the rotor having θ_s,θ_{r1} and θ_{r2} as circumferential coordinates and B_s,B_{r1} and B_{r2} as magnetic flux density respectively, which is illustrated in Figure 4. The magnetic flux density crossing the node located in the stator can be written as a function of the two placed in the rotor by using first order Lagrange interpolation :

$$B_s = \frac{(\theta_s - \theta_{r1})}{(\theta_{r2} - \theta_{r1})} B_{r2} + \frac{(\theta_s - \theta_{r2})}{(\theta_{r1} - \theta_{r2})} B_{r1}. \tag{5}$$

Using the relation between the magnetic flux density and the scalar potential, which is the scalar potential difference multiplied by the permeance and divided by its cross section, given in Eq.(6):

$$\frac{\Delta U_s}{R_s S_s} = \frac{(\theta_s - \theta_{r1})}{(\theta_{r2} - \theta_{r1})} \frac{\Delta U_{r2}}{R_{r2} S_{r2}} + \frac{(\theta_s - \theta_{r2})}{(\theta_{r1} - \theta_{r2})} \frac{\Delta U_{r1}}{R_{r1} S_{r1}}. \tag{6}$$

The last equation can be written as matrix system:

$$[M_1][U_{s1}] - [M_1][U_{s2}] - [M_{rtst}][U_{r1}] - [M_{rtst}][U_{r2}] = 0. \tag{7}$$

With $[U_{r1}\ ]\ [U_{s1}]$ are the vectors containing rotor and stator potentials corresponding to the nodes located at the sliding surfaces and $[U_{r2}\ ]\ [U_{s2}\ ]$ contain the rotor and stator first scalar potential located below/above the sliding surface. $[M_{rtst}]$ is the modified interpolation matrix, in which every element is divided by the reluctance connected to and its cross section, while $[M_1]$ is the matrix containing the permeance of the element divided by its cross section for each element.
It is clear that the movement can be taken into consideration easily, since the number of nodes is fixe and it is only a question of interpolating the scalar potential and the magnetic flux density at the sliding surface.

2.2 Taking into consideration the non-linearity of soft magnetic materials

Generally for this kind of machine the magnetic circuit of the machine is saturated. This last information deviates us to take into consideration the non-linearity of soft magnetic material, in fact assuming that the magnetic characteristic B(H) of steel is linear will reduce the accuracy of results and can lead the designer to a false path. To take into consideration the non-linearity many methods exists such as : Newton-Raphson algorithm or the secant method. The method chosen in our model is the fixed point one, consisting of initializing the non-linear relatives permeabilities with a given value; in our case it is equal to 1500. After that a first resolution is done and then the magnetic field is computed in the structure. From this last one the new permeabilities will be provided from the B(H) curve data of the M330-35A steel followed by the computation of a relative error which is the difference between new permeabilities and old ones. If the error is under a given value, the algorithm will stop, the reluctance matrix will be stored and the rotor position will be incremented if needed. Otherwise, the old permeances matrix will be replaced with a new one computed via the permeabilities and a new global system will be solved again.

3 Lumped parameter thermal model (LPTM)

Lumped model is based on the transformation of thermal problem into an equivalent electrical circuit one, where the heat flow is the current and the nodal temperature is the voltage. The mesh density can vary from a region to an other, where in regions such as slot can be dense and relaxed in iron for example, this will allow the reduction of the total system matrix size and thus accelerate the computation process. In short, each element in the machine is assigned to a thermal resistance and capacitor depending on the material constituting it as shown in Figure 5, its geometrical parameters and the transfer mode (convection or conduction)

$$-[C]\frac{\partial[T]}{\partial t} = [P][T] - [E], \tag{8}$$

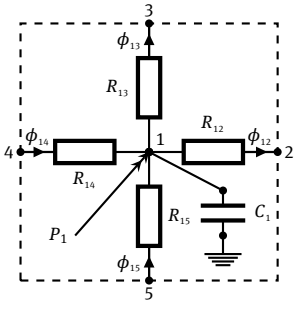

Figure 5: Representation of elementary block for transient thermal computation

$$\left[\Delta t[P] + [C]\right][T_{n+1}] = [C][T_n] + [E]\Delta t. \tag{9}$$

3.1 Convection heat coefficient computation

Convection occurs when a heat flow is exchanged between a solid surface an a fluid, in electrical machine case this is noticed in the heat transfer in airgap and between external machine surfaces and the surrounding fluid (air or cooling one), which are dependent on exchange surface characteristics (rough of smooth) and fluid flow nature (forced or natural). From the last statement, its is clear that rotor speed represents a major key on the computation of convection heat coefficient in airgap, which can be approached as an annulus volume delimited by two cylinders, where one is static and the other is rotating with a constant speed. The appropriate technique to approximate it is by using full computational fluid dynamics analysis, which will demand resources and thus increases computation time. An other method can be used through correlation, such as in [6] by using Taylor's modified number T_{a_m} through geometrical and physical data as can be illustrated in (10), (11), (12) and (13) .

$$T_{a_m} = \frac{\omega^2 R_m e^3}{\nu^2}\frac{1}{F_g}, \tag{10}$$

$$R_m = \frac{e}{\log(\frac{R_2}{R_1})}, \tag{11}$$

$$F_g = \frac{\pi^4}{1697P}\frac{R_1 + R_2}{2R_1}, \tag{12}$$

$$P = 0.0571(1 - \frac{0.652e}{R_1}) + 0.00056(1 - \frac{0.652e}{R_1})^{-1}. \tag{13}$$

Once the Taylor's modified number calculated, the Nusselt's number can be determined through the correlation given in (14) and thus the heat transfer coefficient could be estimated using (15)and (14).

$$\begin{cases} \text{if } T_{a_m} > 1800 \text{ and } T_{a_m} < 10^4 \\ N_u = 0.064 T_{a_m}^{0.367} \\ \text{if } T_{a_m} > 10^4 \text{ and } T_{a_m} < 4\,10^6 \\ N_u = 0.205 T_{a_m}^{0.241} \end{cases} \tag{14}$$

$$h = \frac{N_u\, k_{air}}{2\, E}. \tag{15}$$

3.2 Slot's equivalent conduction coefficient

Conduction heat coefficient in slots determination is deep chalenge, since it is made of a mix several materials, where some are good heat conductors such as copper and the rest are bad at heat transfer like insulator, slot liner, impregnation and residual air. In this work and equivalent coefficient will be computed through slot's section S_{slot}, perimeter l_{sp}, its interior area A_{slot} and its filling factor k_f. Eqs. (16), (17) and (18) illustrate the computation of the slot's thermal resistor and its corresponding coefficient[7]:

$$k_{equi} = 0.1076\, k_f + 0.029967, \tag{16}$$

$$R_{slot} = t_{eq}\,(k_{equi}\, A_{slot})^{-1}, \tag{17}$$

$$t_{eq} = (1 - k_f)\, S_{slot}\, l_{sp}^{-1}. \tag{18}$$

4 Lumped parameter mechanical model (LPMM)

In lumped mechanical model the sub-volumes of the mechanical structure, are modeled by a number of lumped masses or rigid bodies connected by massless elastic and damping elements, such as the springs and resistances. The basic principle involved in such simplifications is that a change of the displacement is considered equal and simultaneous for each element [8]. As in radial rotating machines the circumferential displacements are responsible of high level of noise and vibrations. The developed model is based on a four node 2D isoparametric quadrilateral element having two degree of freedom in x and y directions for each node [9, 10]. Figure 6 illustrates an elementary block in the global coordinates system.

4.1 Element stiffness and mass computation

The basic principle of iso-parametric elements is that the interpolation functions for the displacements are also used to represent the element geometry as in (19). The main use of this formulation is that it makes it possible to generate elements that are non-rectangular having curved sides which is our case for the modeling of cylindrical structures.

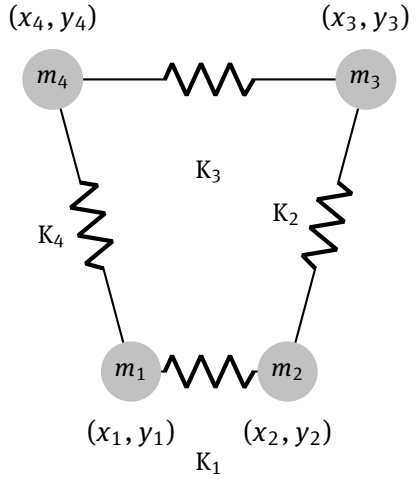

Figure 6: Representation of a mechanical elementary block

$$\begin{aligned} U &= \sum_{i=1}^{4} N_i u_i \quad , \quad V = \sum_{i=1}^{4} N_i v_i \\ X &= \sum_{i=1}^{4} N_i x_i \quad , \quad Y = \sum_{i=1}^{4} N_i y_i \end{aligned} \tag{19}$$

The isoparametric element is then defined in a generalized coordinates system (ζ,η), whith ζ = 1 or -1 and η = 1 or -1. The relation between the cartesian coordinates and the generalised once is insured by the jacobian matrix which link the strain/displacement and or stress/strain as in Eq. (20)

$$\begin{Bmatrix} \frac{\partial N}{\partial \zeta} \\ \frac{\partial N}{\partial \eta} \end{Bmatrix} = \begin{bmatrix} \frac{\partial X}{\partial \zeta} & \frac{\partial Y}{\partial \zeta} \\ \frac{\partial X}{\partial \eta} & \frac{\partial Y}{\partial \eta} \end{bmatrix} \begin{Bmatrix} \frac{\partial N}{\partial \zeta} \\ \frac{\partial N}{\partial \eta} \end{Bmatrix} \tag{20}$$

Using Eq. (19), the jacobian becomes

$$[J] = \begin{bmatrix} \sum_{i=1}^{4} \frac{\partial N_i}{\partial \zeta} x_i & \sum_{i=1}^{4} \frac{\partial N_i}{\partial \zeta} y_i \\ \sum_{i=1}^{4} \frac{\partial N_i}{\partial \eta} x_i & \frac{\partial N_i}{\partial \eta} y_i \end{bmatrix} \tag{21}$$

The N_i are the shape functions at each node of the isoparametric element. Eq. (22) gives their formulation in the generalized coordinates system.

$$N_i = \frac{1}{4}(1 + \zeta_i)((1 + \eta_i)). \tag{22}$$

The displacement can be then approximated in term of the element shape functions by $U = [N]\{d\}$ detailed in Eq. (23), while the strain is approximated using Eq. (24).

$$U = \begin{Bmatrix} u(x,y) \\ v(x,y) \end{Bmatrix} = \begin{bmatrix} N_1 & 0 & N_2 & 0 & N_3 & 0 & N_4 & 0 \\ 0 & N_1 & 0 & N_2 & 0 & N_3 & 0 & N_4 \end{bmatrix} \begin{Bmatrix} u_1 \\ v_1 \\ u_2 \\ v_2 \\ u_3 \\ v_3 \\ u_4 \\ v_4 \end{Bmatrix} \tag{23}$$

$$\epsilon = \begin{Bmatrix} \epsilon_x \\ \epsilon_y \\ \gamma_x y \end{Bmatrix} = \begin{Bmatrix} \frac{\partial U}{\partial X} \\ \frac{\partial V}{\partial Y} \\ \frac{\partial V}{\partial Y} + \frac{\partial U}{\partial X} \end{Bmatrix} = [B]\{d\}. \tag{24}$$

The B matrix is illustrated in (25) where the $\frac{\partial Ni}{\partial x}$ are calculated using the inverse of the jacobian matrix given in (21).

$$[B] = \begin{bmatrix} \frac{\partial N_1(x,y)}{\partial X} & 0 & \frac{\partial N_2(x,y)}{\partial X} & 0 & \frac{\partial N_3(x,y)}{\partial X} & 0 & \frac{\partial N_4(x,y)}{\partial X} & 0 \\ 0 & \frac{\partial N_1(x,y)}{\partial Y} & 0 & \frac{\partial N_2(x,y)}{\partial Y} & 0 & \frac{\partial N_3(x,y)}{\partial Y} & 0 & \frac{\partial N_4(x,y)}{\partial Y} \\ \frac{\partial N_1(x,y)}{\partial Y} & \frac{\partial N_1(x,y)}{\partial X} & \frac{\partial N_2(x,y)}{\partial Y} & \frac{\partial N_2(x,y)}{\partial X} & \frac{\partial N_3(x,y)}{\partial Y} & \frac{\partial N_3(x,y)}{\partial X} & \frac{\partial N_4(x,y)}{\partial Y} & \frac{\partial N_4(x,y)}{\partial X} \end{bmatrix} \tag{25}$$

The element stiffness matrix can be computed using (26), where [D] is the material constraint to deformation linking matrix obtained using the generalized Hook's law $\{\sigma\}$ =

$[D]\{\epsilon\}$. In our case [D] is a [3x3] matrix considering a 2D element having isotropic material properties (27), where A and t are respectively the element area and thickness [11, 12];

$$\begin{array}{c}[K] = \int_{V_e}[B]^T[D][B]dV \\ \text{Since } [B] \text{ is constant} \quad . \\ [K] = [B]^T[D][B]At\end{array} \tag{26}$$

$$[D] = \frac{E}{1-\nu^2}\begin{bmatrix} 1 & \nu & 0 \\ \nu & 1 & 0 \\ 0 & 0 & (1-\nu)/2 \end{bmatrix} \tag{27}$$

The element mass matrix is computed using (28), where ρ is the material mass density.

$$\begin{array}{c}[M] = \int_{V_e}[N]^T[\rho][N]dV \\ \text{Since } [N] \text{ is constant} \\ [M] = [N]^T[\rho][N]At\end{array} \tag{28}$$

An alternative method for the use of numerical integration and to switch from the cartesian coordinates system to the generalized coordinates system knowing that N is function of (ζ, η) is to use the determinant of the jacobian matrix $dV = t.dx.dy = det([J])t.d\zeta.d\eta$.

4.2 Matrix system assembly

The geometry is meshed with a grid of multiple elements having different properties. The problem is to assemble the element matrices into the complete system matrix. Assuming that there is only one unknown at each node the global node numbers will correspond to the global freedom numbers and the element node numbers will correspond to the local freedom numbers. Each element possesses local freedom numbers which follow the standard scheme in 6, namely a consistent clockwise numbering. The global stiffness and mass matrices are obtained by summing the elementary nodal stiffness's and masses of each node shared by several elements, which will necessitate the use of a connectivity matrix. the node numbering is done i a way to obtain a band and symmetric matrices.

4.3 Modal analysis

The equations of motion of a lumped parameter mechanical system can be obtained from Newton's law of motion as in (29).

$$[M]\{\ddot{U}(t)\} + [C]\{\dot{U}(t)\} + [K]\{U(t)\} = \{F(t)\} \tag{29}$$

where [M] , [C], [K], are respectively the structure elements mass, damping, and stiffness matrices. $\{F(t)\}$ is the external forces vector and $\{U(t)\}$ the displacements vector .

In a modal analysis the vibration modes can be obtained by solving the following matrix system in Eq. (30) derived from the generalized equation of motion by assuming harmonic motion, free vibrations and ignoring the damping

$$\left\{[K] - \omega^2[M]\right\} = 0. \tag{30}$$

4.4 Damping matrix computation

In dynamic analysis of elctrical machines damping plays an important role. However due to the limitation in our knowledge about damping, the most effective way to treat damping is to treat the damping value as an equivalent Rayleigh proportional damping [13–15]. The proportional damping model expresses the damping matrix as a linear combination of the mass and stiffness matrices as in Eq. (31)

$$[C] = \alpha[M] + \beta[K] \tag{31}$$

where α and β are damping constant which can be obtained using the orthogonality property of the eigenvectors (mass normalization method) obtained from the modal analysis. In this case, the Eq.(29) becomes uncoupled as in (32) where the second equality gives the (α, β) coefficients in function of the damping ratio which can be obtained experimentally or using the empirical formula (33) as a function of the natural frequencies f_j dedicated to small and medium size electrical machines [16]. The LPMM uses the empirical expression and a curve-fitting algorithm to compute the the unknown (α, β) coefficients that satisfy the maximum modes of the structure.

$$\begin{cases} \ddot{U}_j + 2\xi_j\omega_j\dot{U}_j + \omega_j^2 U_j = P_j \\ 2\xi_j\omega_j = \alpha + \beta\omega_j^2 \end{cases} \tag{32}$$

$$\xi_j = \frac{1}{2\pi}(2.7610^{-5}f_j + 6.210^{-2}). \tag{33}$$

4.5 System reduction

The mass normalization based on the orthogonality of the eigenvectors allows also reducing the size of the system. The eigenvectors of a structural system define the characteristics of the system. Furthermore, the eigenvector associated with the first natural frequencies are the most indicative of the systems dynamics. In many cases, truncating Eq. (29) so that the response of the structure is described in terms of a limited number of eigenvectors does not have a large effect on the overall accuracy of the representation. The advantage is that a problem with a large

number of degrees of freedom can be reduced to a problem with a very small number of degrees of freedom. This can be particularly beneficial where techniques such as time-stepping, which may be computationally expensive, are involved [17].

4.6 Structural transient analysis

Transient dynamic analysis is a study used generally for the determination of a mechanical structure dynamic response due to the action of any time dependent loads. This analysis allows then the determination of the time varying displacements, deformations, stresses, and constraints of a structure as a response to any combination of static, transient, and harmonic loads.

In the general multi-degree-of-freedom case the fundamental equation can be rearranged into the following form.

$$\begin{cases} [M]\{\ddot{U}(t)\} + [C]\{\dot{U}(t)\} + [K]\{U(t)\} = \{F(t)\} \\ Let\ \{Y_1(t)\} = \{U(t)\}; \{Y_2(t)\} = \{\dot{U(t)}\} \\ \{\dot{Y_2}(t)\} = [M]'\{F(t)\} - [M]'[C]\{Y_2(t)\}[M]'[K]\{Y_1(t)\} \end{cases} \tag{34}$$

The discretization of the equations of motion procedure in function of the time variable allow to determine the nodal displacements at different time steps for the studied dynamic system. The direct integration is the most used method in general, it has two classes implicit and explicit. The fist and simplest, is an explicit method known an the central difference method. The second, more complicated but highly efficient than the central difference method known as the Newmark's Beta method (used in many commercial softwares) which model the variation of the acceleration accurately. In our case, The Matlab stiff differential equations solver (ode15s) has been used to solve the matrix system of differential equations Eq. (34). The ode15s is a variable-order solver based on the numerical differentiation formulas.

4.7 Structural harmonic analysis

The Harmonic response analysis is a study used for the determination of the steady-state response of any linear structure to constraints that vary sinusoidally with time. The goal is to calculate the structures response at several frequencies in order to obtain a graphical response versus frequency. The simulations cost of the transient analysis for multiple operating speed leads us the to a structural harmonic analysis.The forced vibrations of the damped structure under harmonic excitation are obtained by solving Eq.35

$$\begin{cases} (-\omega^2[M] + i\omega[C] + [K])U_0 e^{iwt} = \{Fe^{iwt}\} \\ \text{which leads to}: U_0(\omega) = [D]^{-1}F \end{cases} \tag{35}$$

where $[D]$ is the structure impedance matrix. Eq. 36 gives the local displacements amplitude and phase in function of the frequency for each studied mode (j)

$$\begin{cases} U(j) = \sqrt{U_0(j).* U_0^{\star}(j)} \\ \phi(j) = \frac{1}{2i} log(U_0^{\star}(j)./U_0(j)) \end{cases} \tag{36}$$

5 Acoustic model

This section is devoted to the computation of the studied machine emitted acoustic noise. General, a rotating electrical machine can be modeled as one or a combination of acoustic sources such as spheres, cylinders or pistons [18]. In our case the studied motor is modeled as a single sperical monopole acoustic source. The main equation for the evaluation of the radiated sound power is given in 37.

$$W = \rho c \sigma S v^2 \tag{37}$$

where ρc is the air acoustic impedance, S the radiating surface, v the vibration velocity and σ is the radiation ratio which is defined by the radiated sound power of the electric motor in a half space divided by the emitted sound power of equivalent spherical source having the same radiating area and the same vibration velocity as the motor. Thus, the radiation ratio describes the electrical machine sound emission efficiency as compared to the equivalent spherical monopole source. There is multiple formulations in literature [19, 20] to estimate the radiation ratio of a rotary electrical machine depending on its dimensions, mainly the radius to length ratio. In [21], a simplified mathematical expression for the radiation is given as 38.

$$\sigma(f) = 1 - \exp\left(\frac{-2\pi R_e f}{c}\right) \tag{38}$$

where R_e is the machine external radius, f the frequency and c is the speed of sound. The estimation of the machine's emitted noise of electromagnetic origins is then done using Eq. 37 and Eq. 38 along with the maximum magnitude of the vibrating surface mesh nodes. This method may a little inacurate as explained in [22] but it allows to obtain an acceptable over estimated sound power.

6 Models validation and discussions

The validation of the lumped models is done for magnetic computation and modal analysis which allow the derive the structure natural frequencies and their corresponding deformations, a good agreement is obtained compared the FEM results as shown in Figures 12 and 17. The conditions applied for mechanical and magnetic simulation are done using the maximum torque angle and data given in Table 1, derived from a pre-optimization process and chosen randomly from the Pareto front. For further information about mechanical proprieties, one can refer to [23].

6.1 Electromagnetic modeling approach

6.1.1 CFPM Model description

In order to build the electromagnetic model, a ferromagnetic axially laminated steel ($M33035A$) is used for the stator and rotor core magnetic circuit modeling. While, the magnets are modeled as Neodymium-Iron-Boron (NdFeB) with a relative permeability of 1.04 and a remanent field of 1.22 (T).In addition and knowing that the greatest common divisor between the stator slots (30) and the rotor poles pair (3) being equal to 3, the magnetic quantities calculation are performed on only the third of the machine geometry as shown in Figure 1. Once the model is built, the global and local electromagnetic quantities are computed.

6.2 CFPM optimization process

In order to have optimal pre-design parameters selected randomly from the pareto front in Figure 7, Matlab multi-objective genetic algorithm is used as an optimization tool, which is coupled to the multi-physics (magneto-thermal) model in order to compute the maximum delivered torque and hottest slot's spot which define the optimization constraints. Table 2 summarizes the optimization parameters and gives the retained optimization variables: Magnet's thickness ($\boldsymbol{H_{mag}}$) and opening ($\boldsymbol{\theta_{mag}}$), mean radius of the air gap ($\boldsymbol{R_{mean}}$), slot thickness $\boldsymbol{H_{slot}}$ and opening ($\boldsymbol{\theta_{slot}}$), yoke thickness ($\boldsymbol{H_{yoke}}$), machine's active length ($\boldsymbol{L_{act}}$) and current density ($\boldsymbol{J_s}$). The steel used has the characteristic of M330-35A, while magnet loses 8% of their remanent field for each additional 100 [°C] above 20 [°C]. In order to achieve this goal, first, thermal computation will be done in order to estimate machine's hottest spot and after that remanent field will be corrected according to magnet's hottest spot and electromagnetic torque will be evaluated if the machine satisfies thermal constrains, otherwise a penalty will be given to the machine directly.

Table 2: Optimization parameters

Fixed parameters		Constraints	Objective functions
Nominal speed	3000 [rpm]		
Poles / Slots	6 / 30	$\Gamma_{max} \geq 240$[Nm]	$f_1([x]) = \min(\text{Mass}_{PM})$
Winding topology	Penta-Distributed		
Remanent field of PM	1.2	$T_{max} \leq 125$[°C]	$f_2([x]) = \min(\text{Mass}_{machine})$
Airgap	1 [mm]		

Bounds

[0.06; 0.1; 2.5e6; 4.8; 0.025; 0.015; 6; 0.015]
≤[R_{mean}[m]; L_{act}[m]; $J_s[A.m^{-2}]$; θ_{slot}[°]; H_{slot}[m]; H_{yoke}[m]; θ_{mag}[°]; H_{mag}[m]]≤
[0.09; 0.2; 5e6; 7.2; 0.05; 0.03; 18; 0.03]

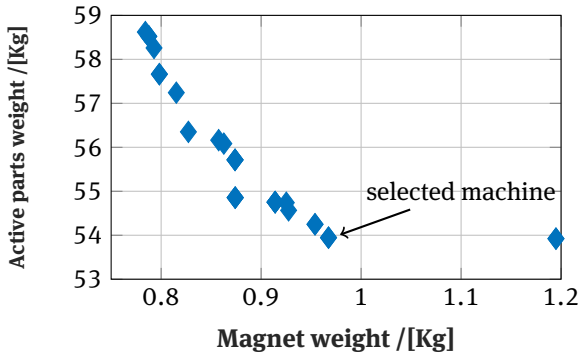

Figure 7: Pareto optimality: optimization results

6.2.1 Local electromagnetic quantities computation

Magnetic flux densities serve to calculate the magnetic pressures for each time step corresponding to its rotor position. Then, a harmonic analysis is performed in order to determine the frequencies of the magnetic load applied on the stator structure. As can be seen in Figure 8, the proposed model estimates the magnetic flux density with a good accuracy compared to FEM ones. Figures 9 and 10 gives respectively the local magnetic forces and their harmonics at load using maximum torque angle.

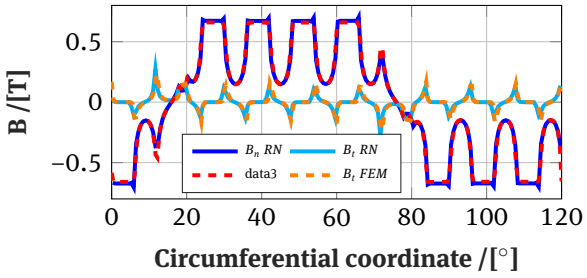

Figure 8: Off load airgap magnetic flux densities distribution

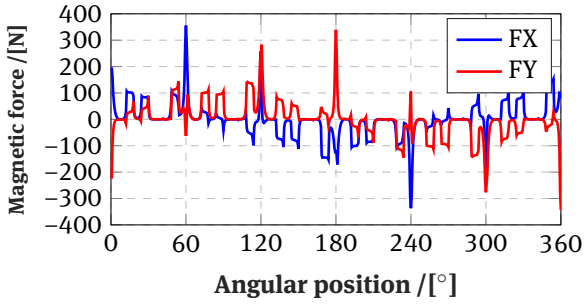

Figure 9: On load airgap magnetic forces distribution

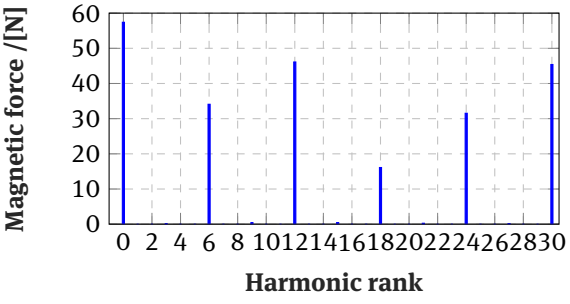

Figure 10: On load airgap magnetic forces harmonics

6.2.2 Global electromagnetic quantities computation

In order to validate the magnetic model, global quantities are compared with those obtained with fem simulation under the same conditions. As can be seen in Figure 11 a good agreement is found between the modeling aproach and fem, also Figure 12 strengthen the previous statement with the load torque comparison, computed using maxwell stress tensor at the middle of the airgap.

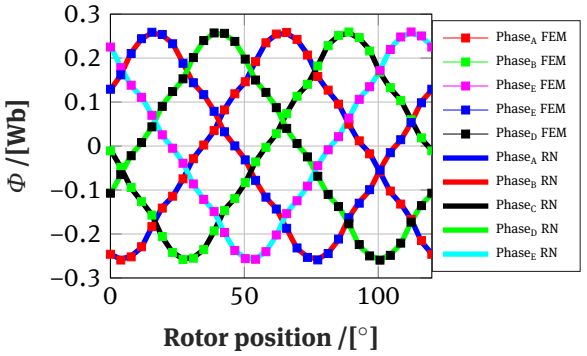

Figure 11: Flux through the phases (No-load)

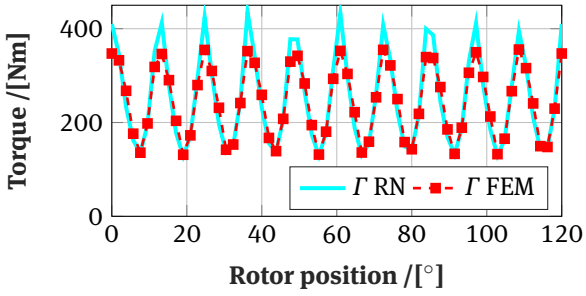

Figure 12: Electromagnetic torque

6.3 Thermal model

The thermal model was validated considering the following assumptions:

1. only conduction and convection are taken into consideration.
2. stator is supposed to be cooled through a liquid with mean temperature of 40 [°] and characterized by a mean convection heat coefficient equal to 400 $[W.m^{-2}.K^{-1}]$.
3. the slot is filled with 60% copper, the rest is supposed to be filled with insulator, residual air and slot's liner.
4. the rotor turn at the nominal speed $\Omega = 3000rpm$.
5. joule losses are first computed at 20$[°C]$, then slot's mean temperature will be estimated and used in order to correct these ones, the processes iterates until the temperature change is under 1%.
6. end windings losses are injected into the slot, in order to reduce the problem to a 2D one.
7. the crankcase is characterized by a thickness equal to 20 [mm] and a conduction coefficient equal to 150 $[W.m^{-1}.K^{-1}]$, while iron conductivity is equal to 50 $[W.m^{-1}.K^{-1}]$ and magnets one to 9 $[W.m^{-1}.K^{-1}]$.

8. transient system is ignored, only steady state system is solved.

Table 3 illustrates the accuracy of the proposed lumped model by comparing its results to FEM one, while Figure 13 illustrates the temperature distribution obtained from the proposed model.

Table 3: Thermal model results validation.

	FEM	Lumped model
T_{slot}	116	118
T_{mag}	102	104
T_{tooth}	108	110

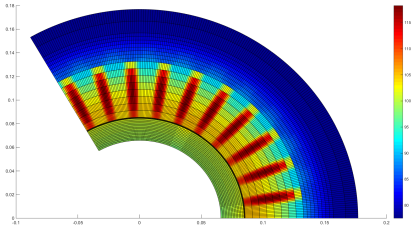

Figure 13: Temperature distribution

6.4 Mechanical modeling approach

The LPMM model is used a first time in a free undamped modal analysis in order to identify the structure natural frequencies and their corresponding deformations. Once natural frequencies are derived, the correlation with the magnetic force harmonics gives the potentially excited vibrating modes. Then, to consider the machine's support in a constrained static analysis which reduce consequently the vibrations magnitude, the LPMM model is used a second time in a structural static analysis for the computation of the displacements for each mode applying loads that have a sinusoidal waveform as indicated in Eq. (39):

$$\begin{cases} P_n(\theta) = \frac{\mathrm{d}F_n}{\mathrm{d}S} = P_{max}\cos(m\theta) \\ P_t(\theta) = \frac{\mathrm{d}F_t}{\mathrm{d}S} = P_{max}\sin(n\theta) \end{cases} \quad (39)$$

where m and n are respectively the circumferential and longitudinal modes number identified in the correlation phase and P_{max} is the maximal magnetic pressure value.

6.4.1 Assumptions

First, only the vibrations of electromagnetic origins are considered. In addition, the noise and vibrations emitted by the rotor are not considered because of their confinement by the stator ones. Second, the mechanical loads are principally located at the airgap stator teeth's. Finally, no rotor eccentricity or unbalance is taken into account. The magnetic forces computed on the airgap stator teeth's faces are used as an entry for the LPMM model which allows to determine the CFPM vibrational behavior due to the applied magnetic loads. The vibration simulations are done for fixed frame at the machine's rated speed of 3000 rpm. The stator magnetic circuit lamination is modeled using equivalent material mechanical properties. By the same way, the windings,end-windings and insulation are characterized by their equivalent properties. The end-bells are not considered in this 2D study. The stator assembly is modeled using the adequate contact coefficients, without keys. Chosen elastic moduli of the different materials are given in Table 4 where, E, G, ν and ρ are respectively Young modulus, shear modulus, Poisson's ratio and mass density. Figure 14 presentes the studied machine meshing and materials affectation.

Table 4: Materials mechanical properties

Parameters	Lamination	Windings	Magnets	Frame
Ex (GPa)	200	9.4	160	71
Ey (GPa)	200	9.4	160	71
Ez (GPa)	0.8	9.4	160	71
Gxy (GPa)	79.3	3.5	64.5	26.7
Gzx (GPa)	0.3	3.5	64.5	26.7
Gyz (GPa)	0.3	3.5	64.5	26.7
ν_{xy}	0.3	0.35	0.24	0.33
ν_{zx}	0.0012	0.35	0.24	0.33
ν_{yx}	0.0012	0.35	0.24	0.33
ρ (kg.m-3)	7700	8890	7500	2700

6.4.2 Taking into consideration the temperature influence on the materials mechanical properties

The vibrational behavior is influenced by the stator temperature. This influence is very difficult to be modeled and quantified as it has a direct impact on the materials mechanical properties of insulations, conductors and the other materials. Generally, for the steel, the Young elasticity modulus is lower when the temperature rises. Contrarily, the Poisson ratio becomes higher with a rise of temperature. In the scientific literature a number of works deal

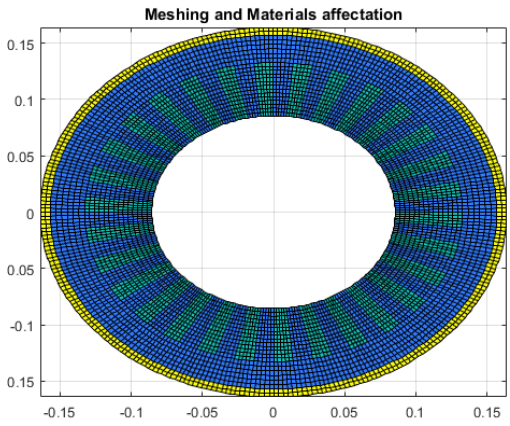

Figure 14: Mechanical meshing and materials affectation

with the problematic of the materials mechanical properties characterization as a function of temperature [24–28]. There are thus simplified physical formulations for the alloys making it possible to obtain the Young's modulus, the shear modulus, and the Poisson's ratio as a function of the temperature such as in [29]. Eq. 40 gives the most used formulation for alloys.

$$E(T) = E_0 - ATexp(\frac{-T_0}{T}) \tag{40}$$

where E_0 is the material Young modulus at 0 Kelvin, A is a tempreature independent constant related to the Grueneisen parameter and T_0 is a characteristic related to Debye temperature ($T_0 = \Theta_D/2$). Unfortunately, this kind of formulations are related to some other parameters which are difficult to obtain and they don't offer good agreements with measurements. For this mean reasons commonly mathematical empirical models based on measurements are used to describes the materials behavior in function of the temperature. In our case and in order to take into account the temperature influence the empirical formulas presented in Eq. (41) for pure steel, copper and aluminum are modified to fit with lamination, windings characteristics and are then used in the LPMM in order to take into consideration the temperature influence in electrical machines, the mechanical properties mathematical model coefficients are given in Table 5 for temperature dependency, in Kelvin, for both Young and Bulk modulus from which one can calculate easily the shear modulus and Poisson ratio. Figures 15 and 16 compare the main mechanical properties between pure iron and laminated steel.

$$y = a + bT + cT^2 \tag{41}$$

Table 5: Temperature dependent Young & Bulk modulus (GPa)

	Lamination		Windings	
	E	B	E	B
a	213.7464	178.6009	10.1981	104.4171
b	0.0119	-0.0218	-0.0022	-0.001
c	$-1.2045\ 10^{-4}$	$7.5229\ 10^{-6}$	$-1.6206\ 10^{-6}$	$-7.5628\ 10^{-7}$

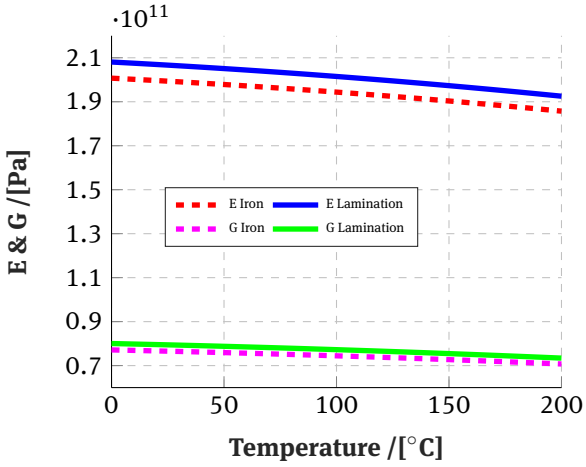

Figure 15: Young and Shear modulus experimental based mathematical model

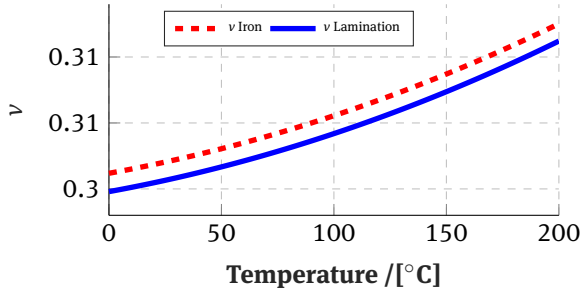

Figure 16: Poisson ratio experimental based mathematical model

6.4.3 Modal analysis

In order to identify the harmonic ranks of magnetic loads responsible for high level of vibrations and noise, a correlation between them and the stator's natural frequencies should be done. To do so, a modal analysis is done in order to derive the structure natural frequencies and their corresponding deformations. Figure 17 gives the comparison between the LPMM and FEA commercial software for the overall natural frequencies of the stator core plus windings and plus the frame. While, Figure 18 gives the corresponding deformation for the circumferential mode num-

ber 2 at a frequency of 1110 Hz, and Figure 19 shows the deformation for the mode number 3 at 2705 Hz. Finally, and to be aware of the temprature influence on the vibrational behavior of electrical machines, Figure 20 shows the temperature influence on the natural frequencies for three different temperatures $20°C$, $100°C$ and $200°C$ respectively, a gap of approximately 100 Hz is noticed from $20°C$ to $100°C$ which is considerable and may induce false conclusions for the CFPM optimization.

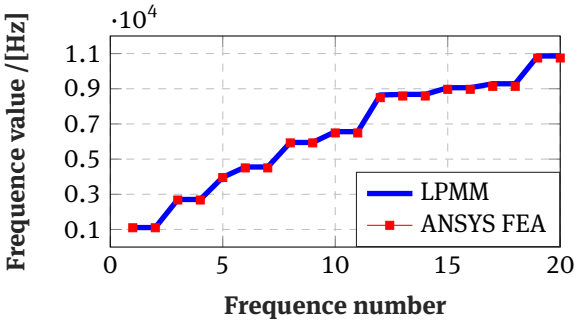

Figure 17: Natural frequencies

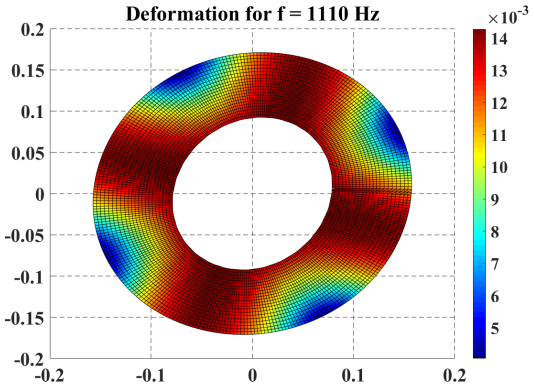

Figure 18: LPMM obtained deformation for mode 2

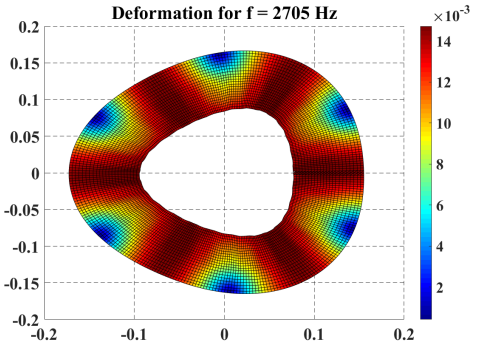

Figure 19: LPMM obtained deformation for mode 3

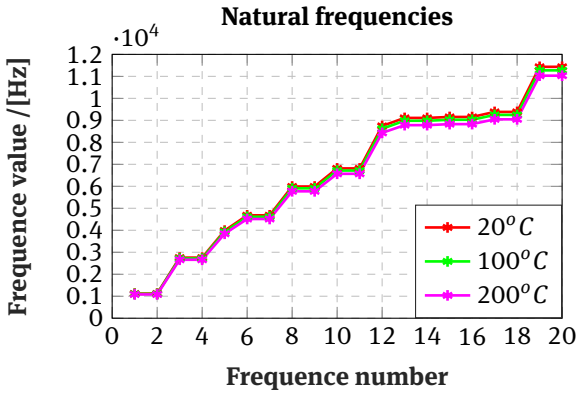

Figure 20: Temperature influence on stator natural frequencies

6.4.4 Transient structural analysis

The validation of the mechanical model for a transient structural response is done for a circumferential mode number 3 at a frequency of 50 Hz which correspond to the rated speed (3000 rpm / 60 = 50 Hz) using Eq. 39. The obtained results are compared to those of a commercial FEA software in Figure 21.

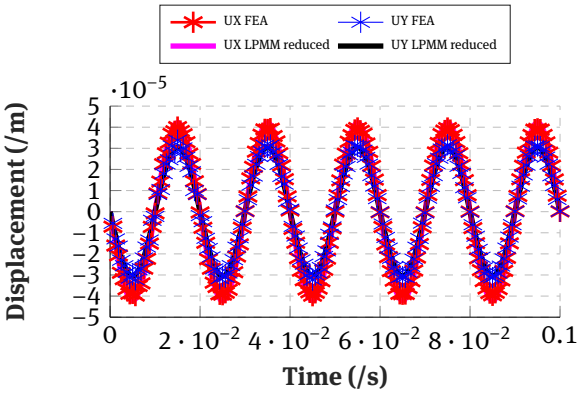

Figure 21: Transient damped displacement on the frame at 90°

6.4.5 Harmonic magneto-vibro-acoustic analysis

The harmonic vibro-acoustic analysis is obtained by a week coupling between the magnetic,mechanic and acoustic models in order to quantify the structure noise emissions due to electromagnetic origins. Figure 22 gives the Sound Pressure Level at 1m distance from the machine for the dominant harmonics of the magnetic forces. One can note that the force harmonic ranks responsible of higher level of vibrations and noise are the rank 0 and rank 6. The highest value is about $75dB_{spl}$ at 4000 Hz followed by an other spike of $60dB_{spl}$ at 9100 Hz. This means that the magnetic force harmonic 0 excites a natural mode

at 4000 Hz and the harmonic 6 excites a natural mode at 9100. So in order to avoid any high level of vibrations and noise one can act first on the harmonics of the magnetic loads at the design stage by changing the structure stiffness. If not, an adequate control canceling or reducing the magnetic force harmonics 0 and 6 can reduce consequently the machines emitted noise.

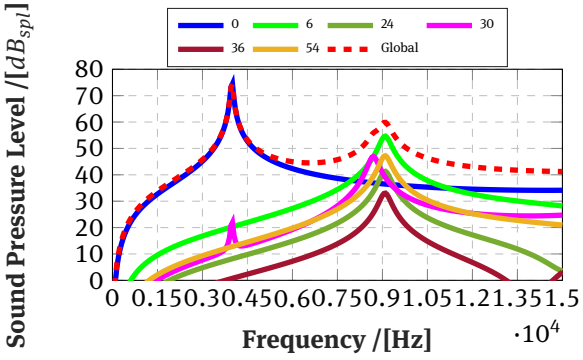

Figure 22: Structure emitted noise SPL

7 Conclusion

Although finite element method is better than lumped parameter models in term of accuracy, they are competitive at the pre-design phase; since they offer acceptable accuracy, being relatively quick and can take into consideration a considerable amount of non-linear phenomenon, which constitutes a powerful tool to investigate large domain and position the designer decision rapidly in the predesign stage as presented in this paper.

Except that obtained results by the lumped models, developed using Matlab programming language, agree with those obtained by the FEM (Flux2D for magneto-thermal part and Ansys mechanical for the mechanical parts), the main goal of this work is to develop computational codes that can be easily coupled and used in a the predesign or optimization phases. One must be careful on the use of this types of models, objectives and especially constraints can change the model choice; as an example: in order to reduce torque ripple, iron losses or voltage harmonics: fem modeling would be preferable, since it is accompanied with less numerical errors and thus more accurate results for such sensitive requirements. However, the obtained pareto front represents a relatively good starting vector for such type of optimization since some first constraints are already fulfilled such as: mean torque and thermal constraints, which will save a tremendous time.

References

[1] Ahmad M.Z., Sulaiman E., Haron Z.A., Kosaka T., Pre- liminary studies on a new outer-rotor permanent magnet flux switching machine with hybrid excitation flux for direct drive ev applications, Power Energy (PECon), 2012 IEEE International Conference, 2012, 928–933.

[2] Benhamida M.A., Ennassiri H., Reluctance network and lumped mechanical models for the modeling of concentrated flux synchronous machine, 18th Int. Symp. on Electromagnetic Fields in Mechatronics, Electrical and Electronic Engineering, 2017.

[3] Mirzaei M., Mirsalim M., Cheng W., Gholizad H., Analysis of solid rotor inductionmachines using coupled analytical method and reluctance networks, Int. J. Appl. Electrom. Mech., 2007, 25, 1-4, 193–197.

[4] Perho J. et al., Reluctance network for analysing induction machines, 2002 Helsinki University of Technology.

[5] Aden A., Amara Y., Barakat Y., Hlioui S., De La Barriere O., Gabsi M., Modeling of a radial flux pm rotating machine using a new hybrid analytical model, Electrical Sciences and Technologies in Maghreb (CISTEM), 2014 Int. Conf. IEEE, 2014, 1–5.

[6] Bouafia M., Bertin Y., Saulnier J., Ropert P., Analyse expérimentale des transferts de chaleur en espace annulaire étroit et rainuré avec cylindre intérieur tournant, Int J. Heat Mass Transf., 1998, 41, 10, 1279–1291.

[7] Staton D., Boglietti A., Cavagnino A., Solving the more dif- ficult aspects of electric motor thermal analysis in small and medium size industrial induction motors, IEEE Trans. on Energy Conv., 2005, 20, 3, 620–628.

[8] Kelly S.G., Fundamentals of mechanical vibrations, 1992.

[9] Ergatoudis I., Irons B., Zienkiewicz O., Curved, isoparametric,“quadrilateral” elements for finite element analysis, Int. J. Solids Struct., 1968, 4, 1, 31–42.

[10] Younis M.I., Vibrations of lumped-parameter systems, in MEMS Linear and Nonlinear Statics and Dynamics, Springer, 2011, 13–56.

[11] Fedder G.K., Simulation of microelectromechanical systems, Ph.D. dissertation, 1994, University of California, Berkeley.

[12] Nikishkov G., Introduction to the finite element method, University of Aizu, 2004.

[13] Chowdhury I., Dasgupta S.P., Computation of rayleigh damping coefficients for large systems, The Electr. J. Geotechn. Eng., 2003, 8, 0, 1–11.

[14] Adhikari S., Damping models for structural vibration, Ph.D. dissertation, 2001, University of Cambridge.

[15] Pilkey D.F., Computation of a damping matrix for finite element model updating, Ph.D. dissertation, 1998.

[16] Yang S., Low-noise electrical motors, 1981, Oxford University Press, USA.

[17] Kim K.-O., Anderson W.J., Generalized dynamic reduction in finite element dynamic optimization, AIAA J., 1984, 22, 11, 1616–1617.

[18] Norton M.P., Karczub D.G., Fundamentals of noise and vibration analysis for engineers, 2003, Cambridge university press.

[19] Beranek L.L., Ver I.L., Noise and vibration control engineering-principles and applications, 1992.

[20] Bösing M., De Doncker R.W., Acoustic modeling of electrical drives: noise and vibration synthesis based on force response superposition, Lehrstuhl und Institut für Stromrichtertechnik

und Elektrische Antriebe, Tech. Rep., 2014.
[21] Wilamowski B.M., Irwin J.D., Power electronics and motor drives, 2016, CRC Press.
[22] Torregrossa D., Peyraut F., Fahimi B., M'Boua J., Miraoui A., Multiphysics finite-element modeling for vibration and acoustic analysis of permanent magnet synchronous machine, IEEE Trans. Energy Conv., 2011, 26, 2, 490–500.
[23] Ennassiri H., Dhifli M., Chabour F., Barakat G., Amara Y., Zidat F., Magneto-vibro-acoustic analysis of a discoidal switching flux permanent magnet machine dedicated to wind turbine application, in Ecological Vehicles and Renewable Energies (EVER), 2016 11th Int. Conf. IEEE, 2016, 1–6.
[24] Adiga V.P., Sumant A.V., Suresh S., Gudeman C., Auciello O., Carlisle J.A., Carpick R.W., Temperature dependence of mechanical stiffness and dissipation in ultrananocrystalline diamond, Micro- and Nanotechn. Sensors, Systems, Appl., 2009.
[25] Ledbetter H., Temperature behaviour of young's moduli of forty engineering alloys, Cryogenics, 1982, 22, 12, 653–656.
[26] McClintock R.M., Gibbons H.P., Mechanical properties of structural materials at low temperatures, 1960, National Bureau of Standards.
[27] Vedrine P., Tixador P., Brunet Y., Bobo J., Fevrier A., Leriche A., Mechanical characteristics of ndfeb magnets at low temperature, Cryogenics, 1991, 31, 1, 51-53.
[28] Van der Giet M., Kasper K., Doncker R.W.D., Hameyer K., Material parameters for the structural dynamic simulation of electrical machines, 2012 XXth Int. Conf. on Electrical Machines, Sept 2012, 2994–3000.
[29] Su D., He Y.-L., Liu J.-Q., Lu X.-G., Establishment of the elastic property database of fe-base alloys, Proc. 1st Int. Conf. on Information Sciences, Machinery, Materials and Energy, 2015.